Desalination 625 (2026) 119913

Contents lists available at ScienceDirect

Desalination

journal homepage: www.elsevier.com/locate/desal

Novel approaches for quantitative assessments of wetting development in membrane distillation based on optical coherence tomography

Nurul F. Himma [a], Harald Horn [a,b], Florencia Saravia [b], Michael Wagner [a,c,*]

[a] Karlsruhe Institute of Technology (KIT), Engler-Bunte-Institut (EBI), Water Chemistry and Water Technology, Engler-Bunte-Ring 9, 76131, Karlsruhe, Germany
[b] DVGW-Research Center at the Engler-Bunte-Institut (EBI), Water Chemistry and Water Technology, Karlsruhe Institute of Technology (KIT), Engler-Bunte-Ring 9, 76131, Karlsruhe, Germany
[c] Karlsruhe Institute of Technology (KIT), Institute of Biological Interfaces (IBG-1), 76344, Eggenstein-Leopoldshafen, Germany

HIGHLIGHTS

- The wetting front development has been successfully detected in situ.
- The spatial distribution of the wetting depth is presented as heat map.
- Wetting was further quantified by wetting ratio and fully-wetted fraction.

GRAPHICAL ABSTRACT

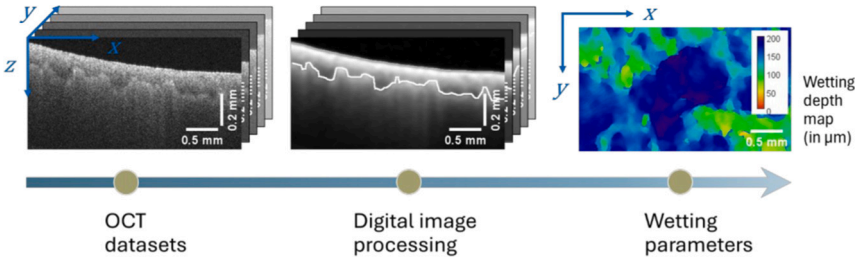

ARTICLE INFO

Keywords:
Heterogeneous wetting
Hydrophobic membrane processes
Membrane distillation
Optical coherence tomography
Wetting front
Wetting quantification

ABSTRACT

Optical coherence tomography (OCT) has been considered as a non-invasive imaging tool to provide real-time, local information of wetting in membrane distillation (MD). However, the follow-up research question is how to quantitatively assess the localized wetting development in order to prevent system failure. This study aims to develop a quantification method based on the changes in the intensity distribution within OCT three-dimensional datasets (volume scan, C-scans). The achieved maps elucidate the wetting depth (e.g., wetting progress) across the membrane area in various cases. Severe wetting with homogeneous and heterogeneous distribution, and even subtle wetting have been quantified successfully. Results indicate that an increase in the volume of wetted membrane (expressed as the wetting ratio) does not necessarily correspond to an increase in the membrane area that is fully wetted (expressed as fully-wetted fraction), revealing the limiting parameter for deterioration in condensate quality. Additionally, the underlying mechanism governing the wetting behavior was also discussed based on the quantified wetting parameters. This OCT-based method would be helpful to investigate wetting not only for MD but also potentially for other membrane processes involving two-phase flow such as gas–liquid membrane contactors and membrane biofilm reactors.

* Corresponding author at: Karlsruhe Institute of Technology (KIT), Engler-Bunte-Institut (EBI), Water Chemistry and Water Technology, Engler-Bunte-Ring 9, 76131, Karlsruhe, Germany.
E-mail address: michael.wagner@kit.edu (M. Wagner).

https://doi.org/10.1016/j.desal.2026.119913
Received 10 November 2025; Received in revised form 16 January 2026; Accepted 24 January 2026
Available online 31 January 2026

1. Introduction

Membrane distillation (MD) has emerged as an attractive desalination process for producing pure water from various water sources such as seawater and wastewater. However, wetting, which is defined as a phenomenon in which the membrane pores are partially or completely occupied by the feed solution instead of water vapor or gases, is the main problem. Wetting is a complex phenomenon influenced by membrane properties, feedwater characteristics, and operating conditions, governing different mechanisms [1,2]. Wetting causes solutes in the feed solution to leak to the condensate or permeate side, deteriorating the quality of the condensate, and the MD will fail to perform separation as the membrane no longer acts as a barrier. Various strategies have been developed to address membrane wetting in MD, including advancements in membrane production, the incorporation of pre-treatments, process optimization, and the development of monitoring techniques [3–7]. Regardless of membrane or process optimization, real-time, in situ wetting monitoring is necessary for improved understanding and effective process control.

Wetting can be detected in situ and non-invasively by measuring the electrical conductivity (EC) of condensate, which has been widely reported in MD studies [8,9]. However, this detection method of wetting is possible after noticeable deterioration in condensate quality (e.g., elevated EC). Moreover, this method is incapable of identifying the location where wetting takes place and determining the actual wetting progress. Several methods have been proposed for early detection of wetting by measuring the generated electrical current in the MD cell equipped with an electrically conductive membrane [10] or an electrically conductive spacer [11]. However, the application of these methods is limited by the material selection, salt concentration, and applied voltage. Furthermore, local-scale information on membrane wetting cannot be obtained.

In the case of wetting, the displacement of water vapor filling the membrane pores by the feed solution can alter the interaction of the incident light with the membrane. Therefore, optical-based methods have been developed for wetting monitoring. Jacob et al. [12] linked an increase in intensity (mean gray value) over a 2D image captured by a camera to wetting propagation since the wetted membrane had a greater light transmission due to refractive index matching (liquid–membrane, compared to air–membrane). The emergence of optical coherence tomography (OCT) as an advanced, non-invasive imaging technology to produce micron-scale resolution images by measuring the echo time delay of light [13] enables detailed observation of wetting development within the membrane cross-section. In contrast to the transmission-based optical method, the signal generated by OCT is based on the light reflected and scattered by the membrane [23,24]. Therefore, less reflection by the wetted parts of the membrane results in decreasing signal intensities. As reported by Bauer et al. [14], wetting led to a narrowing of the membrane signal with irregular fading characteristics. However, no further processing steps were applied to the OCT dataset processing for quantitative wetting evaluation.

Only a few studies reported on using OCT for wetting monitoring and quantification [15,16]. To the best of our knowledge, Shao et al. [15] firstly applied OCT to determine the thickness of the wetted layer in the case of homogeneous wetting, by which the kinetics of surfactant-induced wetting was investigated. The liquid–vapor interface (wetting front) advanced at the same rates along the membrane, and the width between two peaks of pixel intensity was measured as the wetted layer thickness. However, membrane wetting is a non-homogeneous phenomenon, which is influenced not only by the membrane properties (pore characteristics) but also by the process parameters (distribution of concentration, temperature, and pressure along the feed channel) [2,12,17], by which the effects would be more significant in practical applications. Our recent study [18] has successfully visualized heterogeneous wetting development in MD using OCT. Wetting was not homogeneously distributed in the macro- and even meso-scale, emphasizing the complexity in implementing the theoretical classification of wetting [2]. However, it was then accompanied by several issues for quantitative assessments, including (i) the membrane shape, which is not flat and slightly moves in the membrane module, (ii) the wetting itself, which is heterogeneously distributed, and (iii) factors influencing the signal strength and quality. Therefore, systematic and extensive approaches are required.

This work aims to develop methods for quantitative assessment of membrane wetting based on the changes in signal intensities within OCT datasets. The changes in intensity distribution were quantified and analyzed. Therefore, several wetting parameters were defined, including wetting depth, wetting ratio, variability of wetting depth, and fully-wetted fraction. Quantifying these parameters highly relies on accurately identifying the membrane surface and wetting front, for which novel image analysis approaches were developed. The presented parameters allow for the evaluation of wetting distribution and wetting degree, providing local- and global-scale information about the wetting development and mechanism.

2. Materials and methods

2.1. Experimental settings and data acquisition

Air gap MD experiments with CTAB (cetyltrimethylammonium bromide) as the cationic surfactant to induce wetting were performed [18]. Three different cases of wetting corresponding to different conditions of AGMD experiments were investigated in this study. Case I and Case II demonstrated wetting development at a high CTAB concentration (50 mg/L) with the monitoring location was in the middle and near the inlet of the AGMD test-cell, i.e., 12.5 cm and 3.9 cm from the feed inlet, respectively. The feed channel dimensions are 250 mm × 155 mm × 2 mm. Meanwhile, Case III demonstrated wetting development at a low CTAB concentration (10 mg/L) with the monitoring location was in the middle. OCT datasets were acquired using a Ganymede II spectral domain system (Thorlabs, Germany) with a nominal center wavelength of 930 nm. OCT was performed at reference intensities of 68 ± 4%. A-scan averaging was set to seven in order to enhance the signal-to-noise ratio, corresponding to the acquisition time of 1.6 min for the monitored membrane area of 9.40 mm × 3.20 mm with an imaging depth of 2.00 mm. The voxel size is 8 μm × 8 μm × 3.16 μm. Details of the AGMD experimental setup and OCT system are provided in our previous work [18].

Table 1 summarizes the conditions of three AGMD experiments, each representing a different wetting case and consisting of three sequential steps, during which the OCT datasets were acquired. Membrane cross-sections scanned during the first and second steps, operated with deionized water (DI) and 3 g/L NaCl solution, were labeled M0 and M1,

Table 1
Conditions of the different AGMD experiments [18].

C-scan code	Conditions	Case I	Case II	Case III
	CTAB concentration, β_{CTAB}	50 mg/L	50 mg/L	10 mg/L
	Monitoring location (in a 25 cm feed channel)	Middle (12.5 cm)	Near inlet (3.9 cm)	Middle (12.5 cm)
	Operating time			
M0	Step A: DI	3 h (8 ± 1 L/m^2)		
M1	Step B: NaCl (3 g/L)	21 h (64 ± 2 L/m^2)		
M2	Step C: NaCl (3 g/L) + CTAB			
	0 L/m^2	0–2 min	0–2 min	0–2 min
M3	35 ± 6 L/m^2	0.2 h	0.2 h	3 h
M4	82 ± 16 L/m^2	0.3 h	0.3 h	3.5 h
M5	141 ± 16 L/m^2	0.5 h	0.5 h	4.3 h
M6	288 ± 27 L/m^2	1 h	1 h	5 h

CTAB: cetyltrimethylammonium bromide; DI: deionized water. M0–M6 correspond to membrane cross-sections scanned at different stage of experiment.

respectively, and provide a non-wetted baseline with similar cumulative permeate volumes (L/m^2) at fixed operating times of 3 and 21 h. Meanwhile, M2–M6 correspond to scans during operation with CTAB and were selected at comparable cumulative permeate volumes, with operating times varying according to how quickly the EC of permeate approached that of the feed, as described previously [18].

2.2. OCT datasets treatment

Digital image processing was developed to: (i) investigate how changes in intensity distribution correlate with wetting development and (ii) detect the wetting front, from which additional wetting parameters were calculated. These are explained in the following paragraphs.

Fig. 1 illustrates the image processing steps. All steps were performed on 32-bit images. These raw images were first cropped to remove irrelevant objects such as spacer filaments, resulting in 3D images (C-scans) covering a membrane area of 3.36 mm × 1.92 mm, corresponding to 420 × 240 pixels. Macros were programmed in Fiji (based on ImageJ 1.54p [19]) to automate the processing from the raw images until Step II-A and Step III-C. For Step II-B, a Python script was developed.

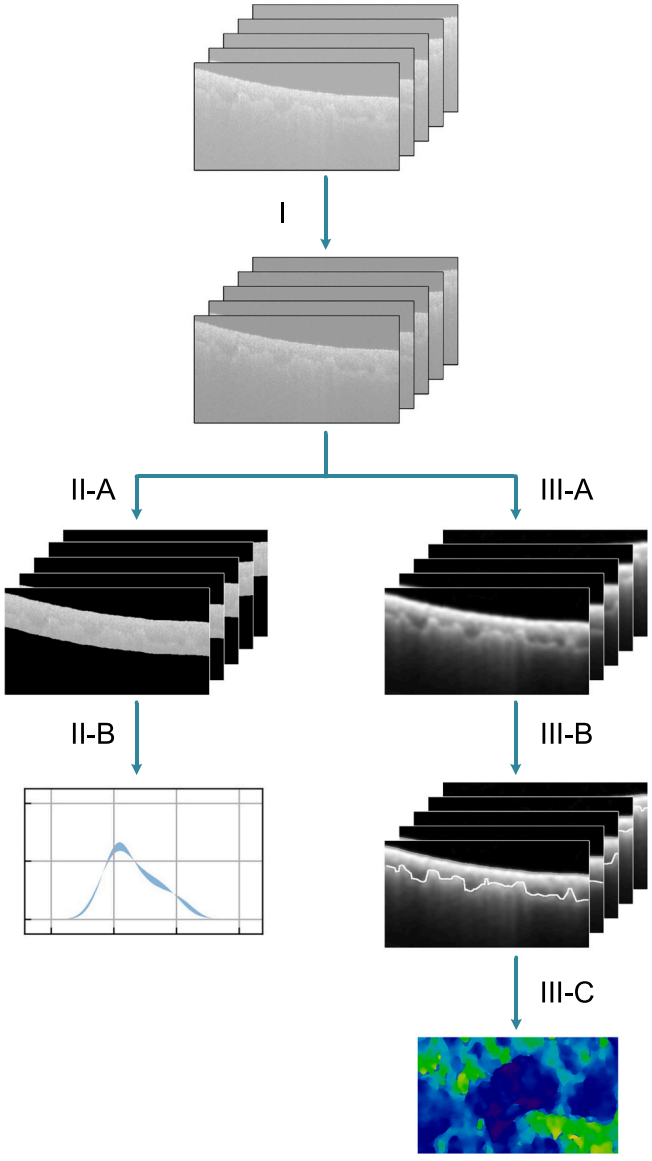

Fig. 1. The digital image processing workflow for wetting evaluation based on intensity distribution (II) and wetting front detection (III). I: intensity normalization. II-A: removal of non-membrane voxels. II-B: calculation of sum of absolute differences. III-A: filtering. Contrast was enhanced only for improved visualization. III-B: tracing membrane surface and wetting front (white line). III-C: generation of wetting depth map.

Step I. The intensities within a volume scan were first normalized to reduce the influence of reference intensity, allowing for the comparison of different datasets. The influence of reference intensity (within the recommended range, i.e., 60–80%) is presented in Fig. S1 (a). Considering the shift in histograms with the increased reference intensity, intensity normalization was performed by subtracting the minimum intensity within the 3D dataset from each voxel. Here, the minimum intensity resembles a global minimum. In order to calculate it, intensities within the 3D dataset were sorted from the lowest to the highest, and the first 0.1% of the total number of voxels were averaged and used as the minimum intensity. As an example, in a dataset of 10,000 voxels, the minimum intensity equals the average of the 10 lowest intensity values (0.1% of 10,000 = 10). The effectiveness and robustness of this normalization method in reducing the effect of reference intensity variations were shown in Section 1 of the SI.

Step II-A. To ensure a correct wetting analysis based on the intensity distribution (i.e., histogram), the dataset was restricted to voxels related to the membrane only. Therefore, the membrane-bulk interface was detected, and the membrane thickness was limited to 200 μm as the maximum membrane thickness based on our measurements. These 200 μm equal a distance of 63 pixels below the membrane-bulk interface. Voxels outside this region of interest were ignored in further calculations since these were set to not-a-number (NaN).

The membrane-bulk interface (membrane surface) was determined using the intensity derivative (the rate of change in intensity) instead of the raw intensity values, according to Eq. (1).

$$f'_{ij} = \frac{f_{ij+1} - f_{ij-1}}{2} \tag{1}$$

where f and f' are the intensity (pixel value) and the first derivative, respectively. The local membrane surface was then identified for each A-scan i as the point j corresponding to the greatest change in intensity.

Step II-B. Dataset M0 (confer Table 1) was used as the reference (initial state). Histograms of M1 – M6 were compared to M0. The sum of absolute differences (SAD, see Eq. 2) was determined as a quantitative measure of the difference between two intensity distributions (e.g., histograms), computed by summing the absolute differences in relative frequencies of intensities between two histograms. Basically, it is the area between two histograms.

$$\mathrm{SAD} = \sum_{p=1}^{N_I} |h_x(p) - h_0(p)| \tag{2}$$

Here h_x and h_0 denotes the relative frequency in the histogram of membrane x (M1–M6) and the histogram of reference membrane (M0), where p indexes the discrete intensity levels defined by the histogram bins ($p = 1, \ldots, N_I$), and N_I denotes the total number of discrete intensity levels (histogram bins) used to represent the intensity distribution. An intensity range of −5 to 65, with a bin width of 0.2, was used to calculate the SAD of histograms in all cases.

Step III-A. A Gaussian Blur 3D filter was applied to reduce the noise. Contrast was enhanced for improved visualization.

Step III-B. The membrane surface was first detected as described in Step II-A and was identified as the first and highest peak in the intensity derivative. The wetting front was subsequently determined by identifying the second peak in the intensity derivative, which

occurs below the membrane surface. This identification was further constrained by the additional criterion given in Eq. 3.

$$f'_{i,j-1} < f'_{i,j} > f'_{i,j+1} \quad (3)$$

This condition defines a local maximum (peak) of the intensity derivative, where the derivative increases before the peak and decreases after it.

Step III-C. The wetting depth over the monitored membrane area was mapped by assigning the distance of the wetting front to the membrane surface as a value in μm to the corresponding pixel $P_{(x,y)}$ in the xy-plane of the field-of-view (420 px × 240 px). The higher the value, the larger the progression of the wetting front.

2.3. Wetting parameters

In order to quantitatively assess the wetting degree and distribution, in addition to SAD, several parameters are presented (Fig. 2 and Table 2).

The local wetting depth, δ_i, was calculated as the distance between membrane surface and wetting front in a single A-scan (see Fig. 2 (a)) as shown in Eq. (4).

$$\delta_i = z_{w,i} - z_{s,i} \quad (4)$$

where $z_{w,i}$ and $z_{s,i}$ are the distances of the wetting front and membrane surface from the top ($z = 0$) at the location i, respectively.

The average wetting depth, $\bar{\delta}$, as the ratio of the wetted membrane volume, V_{WL}, to the monitored membrane area, A_M, can then be expressed as follows.

$$\bar{\delta} = \frac{V_{WL}}{A_M} = \frac{1}{N_A}\sum_{i=1}^{N_A} \delta_i \quad (5)$$

where N_A is the number of A-scans.

The spatial variability of wetting depth, σ^*, was calculated as the mean absolute difference of the local wetting depth and the average wetting depth (as illustrated in Fig. 2 (c)) was calculated using Eq. (6).

$$\sigma^* = \frac{1}{N_A}\sum_{i=1}^{N_A} |\delta_i - \bar{\delta}| \quad (6)$$

Similar to the absolute roughness applied to characterize the fouling structure [20,21], this parameter is presented in this work to evaluate the heterogeneity of wetting distributed across the monitored membrane area.

The wetting ratio ω, defined as the ratio of the wetted membrane volume to the total monitored membrane volume (see Fig. 2 (b)), was calculated as follows.

$$\omega = \frac{V_{WL}}{V_M} = \frac{\sum_{i=1}^{N_A}\delta_i}{N_A \times \delta_m} = \frac{\bar{\delta}}{\delta_m} \quad (7)$$

Table 2
Investigated parameters for wetting evaluation.

Parameter		Definition	Image processing step
Sum of absolute differences	SAD	The area between two histograms	II
Local wetting depth	δ_i	The distance between membrane surface and wetting front in a single A-scan (8 μm in width)	III
Average wetting depth	$\bar{\delta}$	The average distance between membrane surface and wetting front within C-scan	III
Spatial variability of wetting depth	σ^*	The average deviation of the local wetting depths relative to the average wetting depth	
Wetting ratio	ω	Proportion of the membrane that is wet; ratio of the wetted membrane volume to the total monitored membrane volume	III
Fully-wetted fraction	θ	The fraction of the membrane area over which the pores are fully wetted	III

where δ_m is the membrane thickness. This parameter represents the degree of wetting (wetting extent) over the monitored membrane. However, in the case of heterogeneous wetting, this parameter cannot provide information on whether any individual pore is entirely wetted throughout its structure, or on the extent to which local pore wetting has led to liquid leakage into the permeate side.

Therefore, another parameter, fully-wetted fraction, θ, is presented in this work, which was calculated as follows.

$$\theta = \frac{1}{N_A}\sum_{k=1}^{P} k \;\; \delta_k \geq \delta_m \quad (8)$$

where P is the number of A-scans where the membrane cross-section is fully wetted (the entire pore length or membrane thickness is wetted, i.e., the $\delta_k \geq \delta_m$). Since the terms of fully-wetted here is applied to each A-scan (each local unit of pores within 8 μm × 8 μm membrane area), this is different with what called as "fully wetting" or "completely-wetted" or "wetted" in the common classification of membrane wetting degrees [2,7,22] which is applied to the entire membrane, meaning that all membrane pores are completely wetted.

3. Results and discussions

3.1. Wetting development quantified based on changes in the intensity distribution

Fig. 3 (a) compares the intensity distribution in unwetted and wetted membranes monitored at different times (confer Table 1, M0 to M6) for Case I. Wetting was according to Himma et al. [18] expected as the

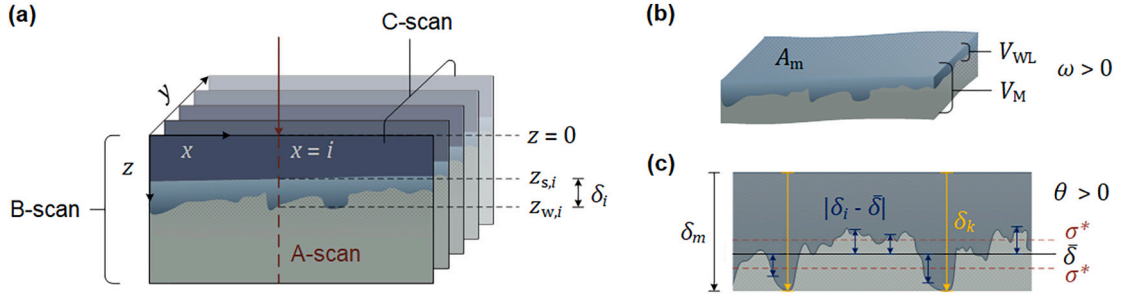

Fig. 2. Schematic illustration depicting (a) local wetting depth, δ_i, as the distance between wetting front, $z_{w,i}$, and membrane surface, $z_{s,i}$, for an individual A-scan within a C-scan, (b) wetting ratio, ω, as the ratio of the wetted membrane volume, V_{WL}, to the total monitored membrane volume, V_M, with A_m is the monitored membrane area, and (c) spatial variability of wetting depth, σ^*, and fully-wetted fraction, θ with δ_m is the membrane thickness.

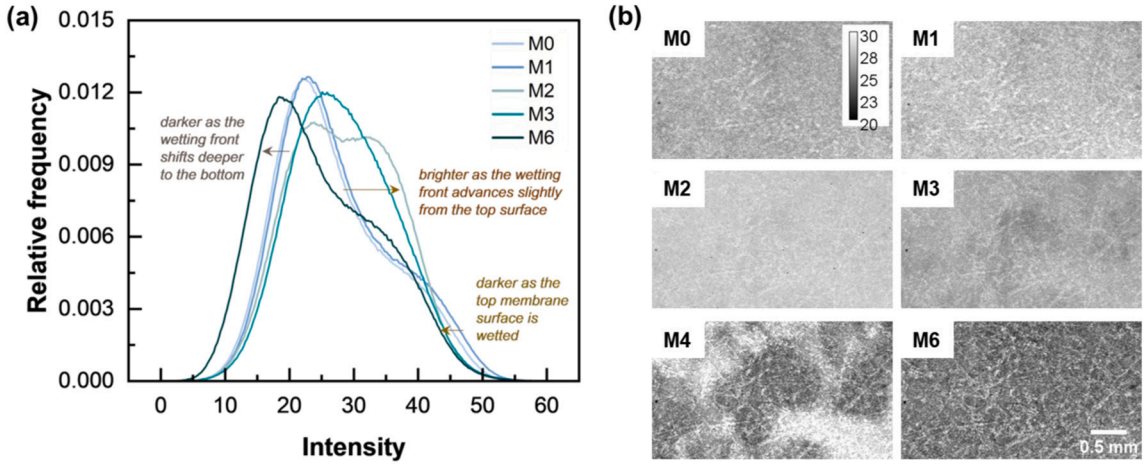

Fig. 3. Presented is Case I (confer Table 1). Changes in the intensity distribution within C-scans due to wetting are shown as (a) histograms and (b) across the scanned membrane area. In (a) the data was obtained using Fiji's stack histogram. In (b) the depicted intensity (mind the calibration bar) equals the arithmetic mean of the A-scan at the corresponding location $i_{(x,y)}$. Membrane area: 3.36 mm × 1.92 mm; membrane thickness = 200 µm. Scale bar (white horizontal line in M6) equals 0.5 mm. Scale and calibration bars apply to all images.

surfactant concentration in Case I was elevated (β_{CTAB} = 50 mg/L). Overall, there was a decline in the relative frequency of higher intensities. At certain times of operation (demonstrated by M2 and M3), this shift was accompanied by the appearance of signal intensities in the range of 25 to 40. It is assumed that this observation was associated with the displacement of the wetting front. At longer operation time (M6), the histogram mainly shifted – as expected – to the left, signifying the drop in light reflection due to wetting and weakening of signals due to stronger light attenuation in higher scanning depths. This is illustrated in Fig. 3 (b), which shows a map of the average A-scan intensity at each location i (x,y) across the scanned membrane. It can be seen that the entire monitored membrane area of M2 became brighter compared to M0. Brighter and darker regions were then observed in M3 and M4, whereas M6 appeared almost entirely dark.

Evolution of the intensity distribution for states M1 – M6 in comparison to M0 is presented in Fig. 4. The blue-shaded region is the area between two histograms and thus equivalent to the progress in wetting. The calculated SAD is shown in brackets (confer Eq. (1)). For Case I, the SAD in M4 first declined, then elevated again. This is ascribed to loss of signal strength as a function of depth. At a certain depth, the intensity of the wetting front diminished to a level accompanied by changes in the surrounding parts, reducing the overall difference. Basically, the signal-to-noise ratio becomes too weak, and hence, determining the actual wetting degree is negatively affected.

In contrast to Case I, SAD in Case II increased continuously. This is due to the greater progress in wetting, resulting in a higher overall difference in intensity. The higher SAD observed in Case II is in agreement with qualitative observations and supported by ex-situ measurements, indicating that wetting was more pronounced near the inlet than in the middle [18]. Interestingly, even slight wetting in Case III was also quantified by the SAD.

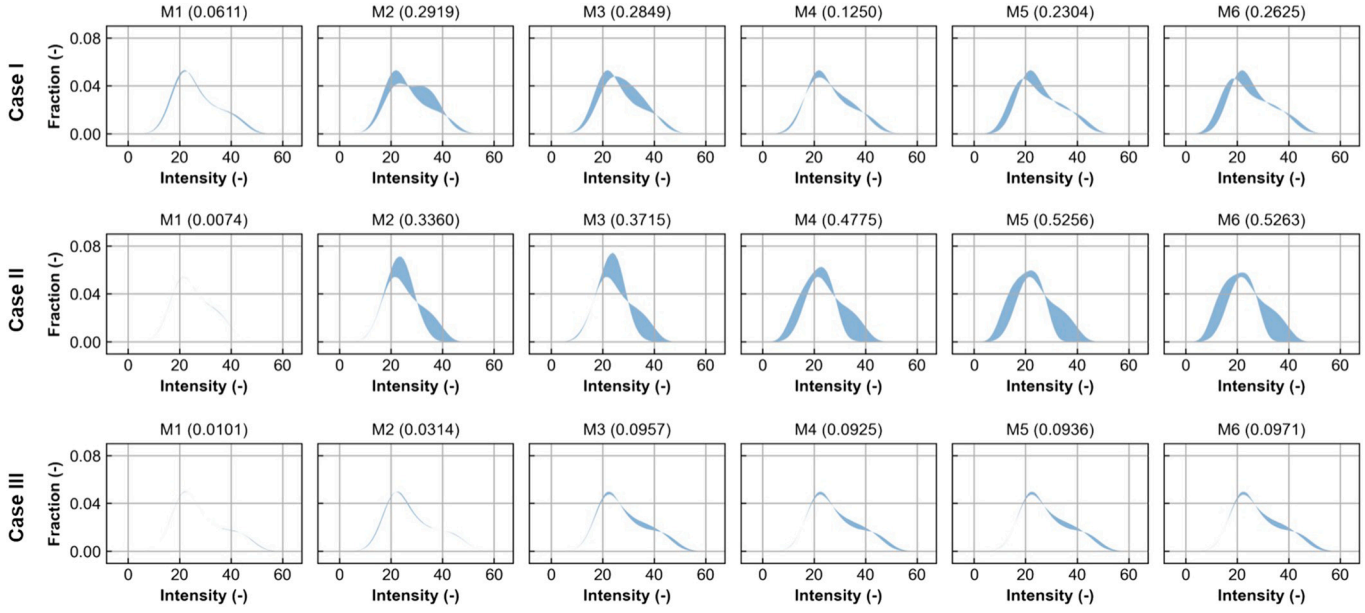

Fig. 4. Differences in intensity distribution within 3D cross-sectional OCT images scanned at different times (M1 to M6, confer Table 1) compared to the initial unwetted state (M0) for all cases. The calculated sum of absolute differences (SAD) is shown in brackets. ROI: 3.36 mm × 1.92 mm with a depth of 200 µm from the membrane surface.

3.2. Wetting development quantified based on the displacement of wetting front

A series of A-scans illustrating the change in intensity distribution with progressing operational time for Case I (see Table 1 for experimental details) is shown in Fig. 5 (a). The A-scan (Fig. 5 (a) – M0) starts with a smooth intensity distribution over depth. The peak at approximately 0.13 mm marks the surface. Due to light attenuation, the signal intensity decreases over depth. A similar profile was exhibited by M1, meaning that after operation with NaCl feed for 21 h, the membrane properties remained unchanged, and no wetting occurred. The effect of wetting is shown in Fig. 5 (a) – M2 to M6, where an additional peak appears. This peak indicates the displacement of the wetting front within the membrane.

The distance between the membrane surface and the wetting front indicates the progression of the wetting. However, determining this distance from intensity peaks was challenging due to inconsistencies in the membrane surface signal under wetting. In cases of slight wetting, the membrane surface often exhibits lower intensity than the wetting front, making membrane surface detection based on the highest signal intensity can be misleading. Additionally, the peaks are broad with variations in the baseline level, further complicating accurate detection. To overcome these issues, the membrane surface was identified as the point of maximum intensity change, calculated as the first derivative of an A-scan. This approach provided accurate and consistent results. As shown in Fig. 5 (b), the membrane surface peaks were symmetrical and consistently represented the global maximum of the intensity derivative in the A-scan.

While the membrane surface was represented by the global maximum of the intensity derivative, the wetting front was then represented by the highest peak of intensity derivative detected within the membrane thickness. The peaks of the wetting front were also symmetrical and more distinguishable (Fig. 5 (b)). This approach was highly effective in detecting the wetting front, allowing for the calculation of wetting depth. However, some challenges were found in cases where wetting occurred to a depth within the range of the total membrane thickness. The challenges arose from a weakening signal-to-noise ratio and an unknown local membrane thickness. In addition, the A-scan profile of fully-wetted spots showed a similar pattern to the unwetted ones, in which there was no peak of wetting front detected within the membrane thickness. The developed image analysis routines account for such inconsistencies (see SI, Section 2). First, a better membrane thickness determination was performed to address local variations which are not covered by the manufacturer's specification. Here, the average membrane thickness was 178 μm (corresponding to 56 pixels), with the minimum and maximum thickness of 146 μm and 200 μm (corresponding to 46 and 63 pixels), respectively. Second, a maximum intensity (along the A-scan) of 40 was set as the upper limit to consider that the peak detected between the minimum and maximum membrane thickness did not represent a (nearly) unwetted state, and a maximum intensity of 27 was applied as the upper threshold required for a fully-wetted state (the maximum membrane thickness was assigned as the wetting depth). In the absence of wetting front detected with higher intensities (>27), a change in the distance of the highest intensity from the actual membrane surface detected based on intensity derivative relative to the initial condition (the minimum distance representing unwetted state) was considered as the wetting depth. This approach was effective not only to identify unwetted states but also to account for slightly wetted states with merged peaks due to the applied filter. As demonstrated in Fig. 5 (c) and **Fig. S3**, the detection of the wetting front is in strong agreement with the visual observations. The local wetting depths were able to be determined regardless of the membrane shape and wetting pattern (e.g., smooth form, slight waviness, or irregular variations in the wetting fronts).

Successful wetting depth determination merged into heat maps showing the wetting distribution across the monitored membrane area.

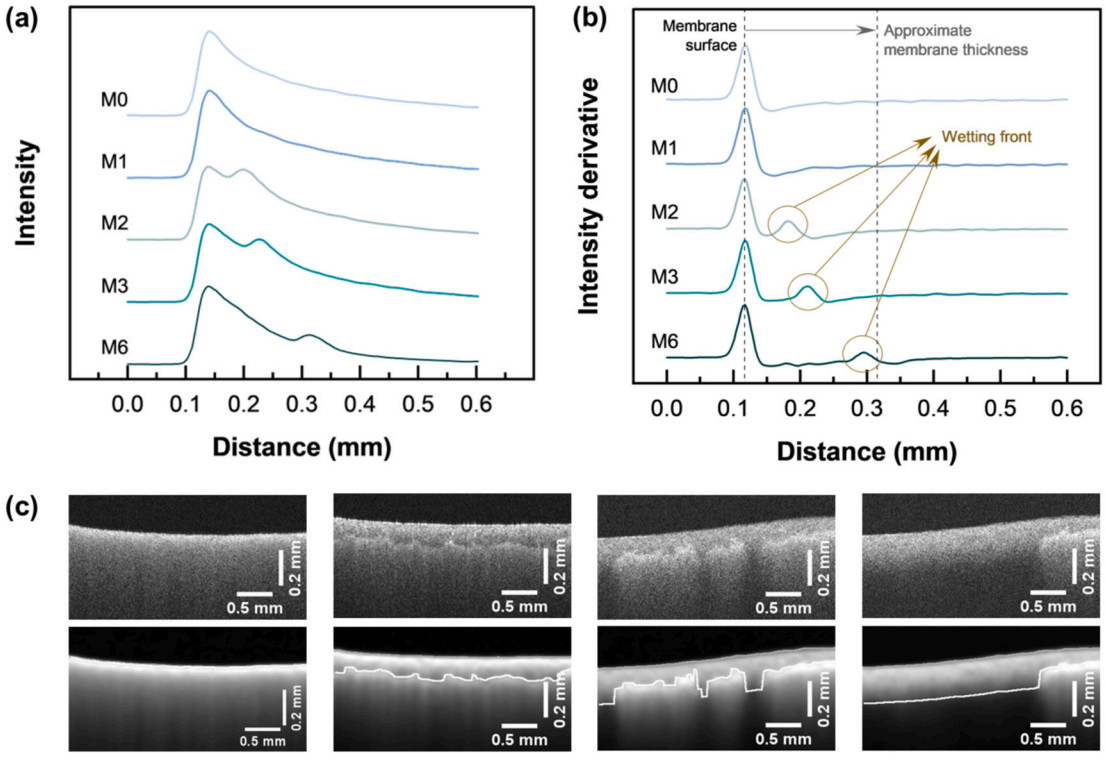

Fig. 5. Presented is Case I (confer Table 1): (a) A representation of development in intensity profile along A-scan path due to wetting and (b) the corresponding derivative or rate of change in intensity. (c) B-scans showing the tracing of wetting front along the monitored membrane with different wetting patterns (from left to right: Case I – M0 and M3, Case II – M3 and M4), indicated by the white line, compared to the initial B-scans (the first row). The line of wetting front is shown in white color.

Wetting depth development is presented in Fig. 6. It provides an overview of the different Cases I, II, and III (confer Table 1) studied here. Overall, consistent results were achieved for the practically unwetted membrane (M0 and M1 in all cases). It was measured that the wetting front was displaced to 5–10 μm on average from the membrane surface. At the beginning of operations with a high surfactant concentration of 50 mg/L (Cases I and II – M2), wetting was evenly distributed across the membrane with an average wetting depth of ~70 μm. After that, wetting in some parts of the membrane progressed more rapidly compared to other parts, and fully-wetted parts, indicated by the dark blue spots, were observed. The dark blue spots expanded over time in both cases, and as observed in M6, nearly the entire membrane area became fully-wetted. However, compared to Case I, wetting progress in Case II was more abrupt and exhibited greater spatial heterogeneity. Meanwhile, wetting developed extremely slowly in operation with a low surfactant concentration of 10 mg/L (Case III). Over the entire period with surfactant (from M2 to M6), the wetting front advanced from 9 to 17 μm on average from the membrane surface. The wetting depth maps confirm quantitatively what has been shown in previous work [18], and it will be further discussed in the following section.

3.3. *Wetting parameters and mechanism analysis*

Wetting parameters based on the wetting front detection were used

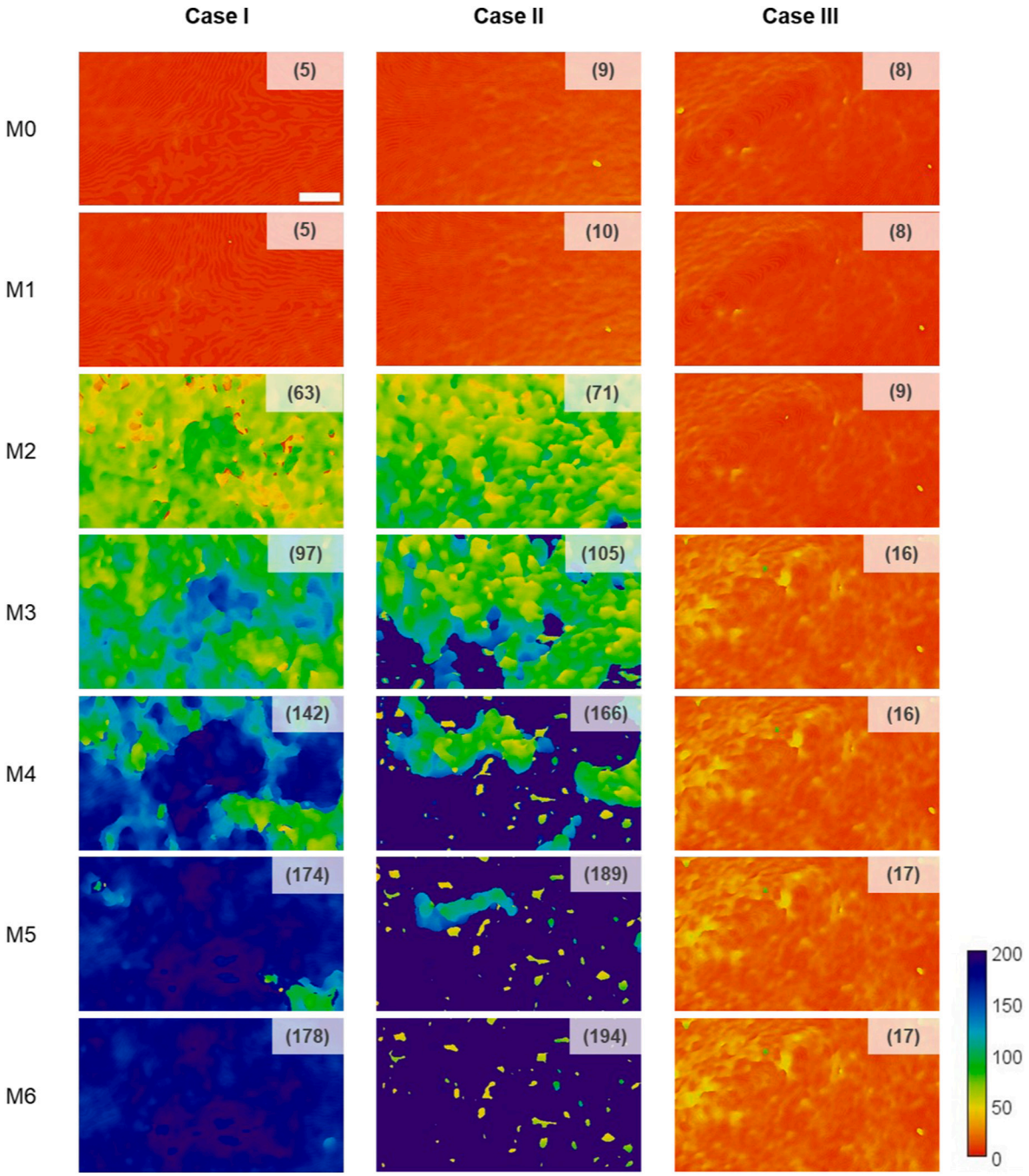

Fig. 6. Distribution of wetting depth over time in Case I, Case II, and Case III, calculated based on the detected wetting front. The calibration bar shows the wetting depth in μm. Thus, no wetting is shown in red, while complete wetting is shown in dark blue color. Scale bar (white horizontal line in Case I - M0) equals 0.5 mm. Scale and calibration bars apply to all wetting maps. The calculated average wed depth for each map is shown in brackets.

to elucidate the wetting mechanism and correlate with the process performance. The calculated parameters indicating the development of membrane wetting in MD are shown in Fig. 7.

As shown in Fig. 7 (a), M0 and M1 in all cases exhibited a comparable negligible wetting ratio ω of 0.03–0.05. With the addition of a high concentration of surfactant (from M2), the wetting ratio in Cases I and II remarkably increased to ~0.9, reaching a plateau. This increasing wetting ratio led to an approximately 100-fold increase in flux [18]. This dramatic increase in flux indicated that there was convective flow of liquid replacing the vapor transport, in addition to the reduced path length for vapor transport with the decreased volume (corresponding to the thickness) of the dry portion of the membrane, as demonstrated in a modeling study [23].

Within the first 82 L/m^2 cumulative permeate volume (M4), even though the wetting ratio in Case II developed at a slightly higher rate than that in Case I, Case II experienced a much steeper increase in fully-wetted fraction θ (Fig. 7 (b)). Approximately 70% of the monitored membrane in Case II was fully-wetted, while it was ~20% in Case I. Describing the membrane area through which the liquid feed solution reaches the permeate side, this parameter certainly defined the decline in overall rejection. The rejection drastically declined from approximately 99% to almost zero [18].

At the beginning of operation with surfactant (M2), the spatial variability of wetting depth in Case II was comparable to that in Case I, which was 12 and 10 μm, respectively (see Fig. 7 (c)). Case II then exhibited greater change in the wetting depth variability σ^*, which was twofold higher at the first 35 L/m^2 of the cumulative permeate volume (M3). After reaching 141 L/m^2 (M5 and M6), the wetting depth variability continuously decreased in both cases.

Meanwhile, wetting in Case III developed slowly, characterized by a subtle increase in wetting ratio, rising from 0.04 to 0.08 over the process duration, with the absence of fully wetted regions. This means that 8% of the monitored membrane volume is wetted; however, none of the pores were fully wetted along their entire length. With the wetting depth variability of 5 μm, a maximum of 41% of the pore length was found to be wetted. These results signified the capability of the presented approaches in quantifying surface wetting where the wetting front in all parts was slightly displaced below the membrane surface.

Systematically comparing the quantified wetting parameters in Cases I and II (as depicted in Fig. 7), the wetting development across (through) and along the membrane as well as the underlying mechanism can be explained as follows.

Initial relatively homogeneous surface wetting (observed in M2). It has been well-known that the liquid entry pressure (LEP) is a general criterion for membrane pore wetting, and instantaneous wetting will only occur when the applied pressure exceeds the LEP, which is a function of pore size, liquid surface tension, and contact angle on the membrane surface [24,25]. Since the initial LEP is higher than the applied pressure, the surfactant-induced wetting occurs progressively instead of instantaneously, which is influenced by adsorption. When the feed solution containing a high concentration of surfactant is in contact with the membrane surface, adsorption immediately takes place, altering its surface hydrophobicity. As a result, the whole membrane surface initially gets wet.

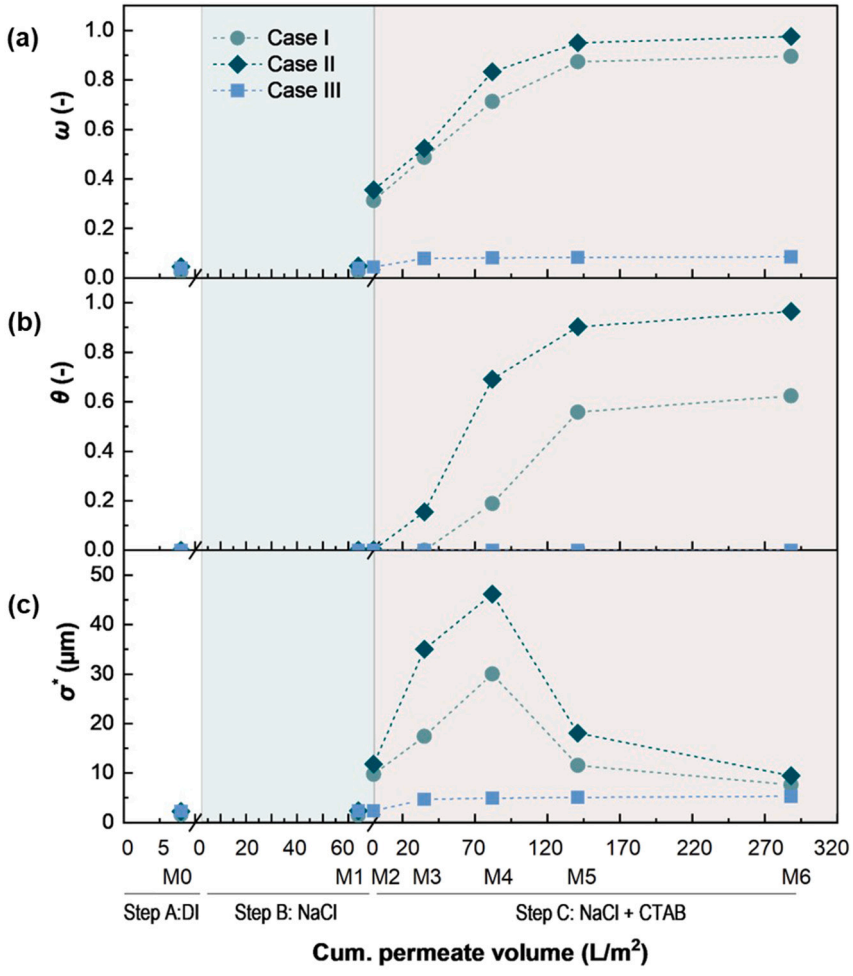

Fig. 7. Wetting ratio, ω, fully-wetted fraction, θ, and spatial variability of wetting depth, σ^*, with the increased cumulative permeate volume in different cases of membrane distillation. The wetting ratio also accounts for voxels corresponding to not fully-wetted parts of the membrane.

Heterogeneous partial wetting (observed in M3–M4). Spatially non-uniform wetting development indicates the heterogeneity in local LEP. In the axial pore direction (across the membrane thickness), the adsorption reduces the surfactant concentration close to the pore surface, increasing local LEP. Further wetting can then be promoted by mass transport of the surfactant to the wetting front to reduce the local LEP. Therefore, as has been proposed by Wang et al. [26], the wetting kinetics is highly influenced by the bulk concentration of surfactant and water vapor flux, determining the diffusive and convective transport of the surfactant. Elaborating this mechanism with the distribution of process parameters and membrane pore structure, it could then be explained that wetting propagation at different rates on the scale of tens to a few thousand microns in axial flow direction (along the membrane) would be predominantly attributed to the membrane pore size distribution, while that on the wider scale would be highly influenced by distribution of bulk concentration, pressure, and temperature along the feed channel. As shown in **Fig. S5**, the membrane used had a wide pore size distribution, governing heterogeneity in local LEP. Even though the distribution was skewed to the smaller pore sizes, approximately half of the pores were evenly distributed in larger sizes. These biggest pores would be responsible for the early fully-wetted fraction by providing the lowest LEPs, regardless of the flow direction. This effect would become less pronounced when the applied pressure is much lower than LEP, which would also be the case with the presence of a pressure drop due to a spacer in the feed channel [18,27]. In addition, synergistic effects, such as the reduction in bulk surfactant concentration due to continuous adsorption (which lowers surface tension and the rate of further adsorption), along with a temperature drop due to conductive and evaporative heat loss [28] (which also reduces surface tension and water vapor flux), would contribute to the decreased wetting with the increased membrane length.

Less heterogeneous nearly-full wetting (observed in M5–M6). Further penetration of the liquid feed through the membrane pores (as indicated by the high wetting ratio) reduces the temperature gradient across the membrane, resulting in the absence of the driving force for water vapor transport. The vapor transport becomes negligible compared to the liquid feed. Since almost no separation takes place, the influence of gradient concentration on the local LEP is negligible, resulting in more homogeneous wetting along the membrane.

4. Conclusion

This work has successfully established an in-situ and real-time quantification method of localized wetting in MD based on OCT, regardless of the membrane shape and wetting heterogeneity. The SAD is generally elevated with the enhanced wetting. However, the results did not allow for estimating a correlation to the wetting ratio. The proposed approach, based on the intensity distribution analysis, effectively detected and quantified the wetting progression and spatial distribution, as expressed by heat maps of the scanned membrane area. The results emphasize that wetting can be distributed unevenly and develop non-linearly over time. The developed method and the presented findings could pave the way for further advancements in understanding membrane wetting in MD. Early detection of the wetting front, prior to complete wetting, would enable improved process control, facilitating membrane regeneration, and thus reducing operational costs. Further studies are needed to evaluate the applicability of this approach under complex wetting–fouling conditions and in other hydrophobic membrane processes involving gas–liquid displacement, such as membrane gas absorption and membrane biofilm reactor.

Declaration of competing interest

The authors declare that they have no known competing financial interests or personal relationships that could have appeared to influence the work reported in this paper.

Acknowledgements

Graduate Funding from the State (LGF) for Nurul F. Himma, awarded by KIT and sponsored by the Ministry of Science, Research and the Arts (MWK) of Baden-Württemberg, is gratefully acknowledged. Scholarship awarded to NFH within the framework of the Graduate Funding from the German States Program ("Landesgraduiertenförderung") from KIT and Ministry of Science, Research and Arts of Baden-Württemberg (MWK) is gratefully acknowledged. KIT Research Laboratories and DVGW Research Center at EBI, Water Chemistry and Water Technology are acknowledged for the support. This work was supported through the Helmholtz Association programme "Materials Systems Engineering" under the topic "Adaptive and Bioinstructive Materials Systems".

Appendix A. Supplementary data

Supplementary data to this article can be found online at https://doi.org/10.1016/j.desal.2026.119913.

Data availability

Data will be made available on request.

References

[1] H. Chang, B. Liu, Z. Zhang, R. Pawar, Z. Yan, J.C. Crittenden, R.D. Vidic, A critical review of membrane wettability in membrane distillation from the perspective of interfacial interactions, Environ. Sci. Technol. 55 (2021) 1395–1418.
[2] M. Rezaei, D.M. Warsinger, J.H. Lienhard V, M.C. Duke, T. Matsuura, W. M. Samhaber, Wetting phenomena in membrane distillation: mechanisms, reversal, and prevention, Water Res. 139 (2018) 329–352.
[3] N.M.A. Omar, M.H.D. Othman, Z.S. Tai, T.A. Kurniawan, M.H. Puteh, J. Jaafar, M. A. Rahman, S.A. Bakar, H. Abdullah, A review of superhydrophobic and omniphobic membranes as innovative solutions for enhancing water desalination performance through membrane distillation, Surf. Interfaces 46 (2024) 104035.
[4] Y. Ye, L. Zhao, Z. Liu, Z. Wang, Q.J. Niu, Recent advances in novel membranes for improved anti-wettability in membrane distillation: a mini review, Desalination 571 (2024) 117066.
[5] A. Abdel-Karim, S. Leaper, C. Skuse, G. Zaragoza, M. Gryta, P. Gorgojo, Membrane cleaning and pretreatments in membrane distillation – a review, Chem. Eng. J. 422 (2021) 129696.
[6] E. Guillen-Burrieza, M.O. Mavukkandy, M.R. Bilad, H.A. Arafat, Understanding wetting phenomena in membrane distillation and how operational parameters can affect it, J. Membr. Sci. 515 (2016) 163–174.
[7] H. Chamani, J. Woloszyn, T. Matsuura, D. Rana, C.Q. Lan, Pore wetting in membrane distillation: a comprehensive review, Prog. Mater. Sci. 122 (2021) 100843.
[8] M. Gryta, Long-term performance of membrane distillation process, J. Membr. Sci. 265 (2005) 153–159.
[9] S. Adham, J. Minier-Matar, A. Hussain, Pilot plant evaluation of membrane distillation for desalination of high-salinity brines, Appl Water Sci 13 (2023) 233.
[10] F.E. Ahmed, B.S. Lalia, R. Hashaikeh, Membrane-based detection of wetting phenomenon in direct contact membrane distillation, J. Membr. Sci. 535 (2017) 89–93.
[11] A. Alpatova, A. Qamar, M. Alhaddad, S. Kerdi, H. Soo Son, N. Amin, N. Ghaffour, In situ conductive spacers for early pore wetting detection in membrane distillation, Sep. Purif. Technol. 294 (2022) 121162.
[12] P. Jacob, B. Dejean, S. Laborie, C. Cabassud, An optical in-situ tool for visualizing and understanding wetting dynamics in membrane distillation, J. Membr. Sci. 595 (2020) 117587.
[13] J. Fujimoto, W. Drexler, Introduction to optical coherence tomography, in: W. Drexler, J.G. Fujimoto (Eds.), Optical Coherence Tomography: Technology and Applications, Springer Berlin Heidelberg, Berlin, Heidelberg, 2008, pp. 1–45.
[14] A. Bauer, M. Wagner, H. Horn, F. Saravia, Operation conditions affecting scale formation in membrane distillation - an in situ scale study based on optical coherence tomography, J. Membr. Sci. 623 (2021) 118989.
[15] S. Shao, D. Shi, J. Hu, W. Qing, X. Li, X. Li, B. Ji, Z. Yang, H. Guo, C.Y. Tang, Unraveling the kinetics and mechanism of surfactant-induced wetting in membrane distillation: an in situ observation with optical coherence tomography, Environ. Sci. Technol. 56 (2022) 556–563.
[16] D. Shi, T. Gong, W. Qing, X. Li, S. Shao, Unique behaviors and mechanism of highly soluble salt-induced wetting in membrane distillation, Environ. Sci. Technol. 56 (2022) 14788–14796.
[17] Y. Luo, S. Shao, J. Mo, Y. Yang, Z. Wang, X. Li, Spatio-temporal progression and influencing mechanism of local wetting in membrane distillation, J. Membr. Sci. 670 (2023) 121374.

[18] N.F. Himma, M. Wagner, H. Horn, F. Saravia, In-situ monitoring and understanding of wetting in membrane distillation by means of optical coherence tomography, Sep. Purif. Technol. 371 (2025) 133203.
[19] J. Schindelin, I. Arganda-Carreras, E. Frise, V. Kaynig, M. Longair, T. Pietzsch, S. Preibisch, C. Rueden, S. Saalfeld, B. Schmid, J.-Y. Tinevez, D.J. White, V. Hartenstein, K. Eliceiri, P. Tomancak, A. Cardona, Fiji: an open-source platform for biological-image analysis, Nat. Methods 9 (2012) 676–682.
[20] K.T. Huisman, B. Blankert, H. Horn, M. Wagner, J.S. Vrouwenvelder, S. Bucs, L. Fortunato, Noninvasive monitoring of fouling in membrane processes by optical coherence tomography: a review, J. Membr. Sci. 692 (2024) 122291.
[21] M. Wagner, H. Horn, Optical coherence tomography in biofilm research: a comprehensive review, Biotechnol. Bioeng. 114 (2017) 1386–1402.
[22] M. Gryta, Influence of polypropylene membrane surface porosity on the performance of membrane distillation process, J. Membr. Sci. 287 (2007) 67–78.
[23] Y. Jin, N. Ghaffour, Understanding the effect of membrane interfacial wetting properties on membrane distillation flux, Desalination 548 (2023) 116260.
[24] B.-S. Kim, P. Harriott, Critical entry pressure for liquids in hydrophobic membranes, J. Colloid Interface Sci. 115 (1987) 1–8.
[25] A.C.M. Franken, J.A.M. Nolten, M.H.V. Mulder, D. Bargeman, C.A. Smolders, Wetting criteria for the applicability of membrane distillation, J. Membr. Sci. 33 (1987) 315–328.
[26] Z. Wang, Y. Chen, X. Sun, R. Duddu, S. Lin, Mechanism of pore wetting in membrane distillation with alcohol vs. surfactant, J. Membr. Sci. 559 (2018) 183–195.
[27] A. Hagedorn, G. Fieg, D. Winter, J. Koschikowski, A. Grabowski, T. Mann, Membrane and spacer evaluation with respect to future module design in membrane distillation, Desalination 413 (2017) 154–167.
[28] J.M. Rodríguez-Maroto, L. Martínez, Bulk and measured temperatures in direct contact membrane distillation, J. Membr. Sci. 250 (2005) 141–149.